Annual Report

The Use of 4-Dimensional Lidar Data to Evaluate Large Eddy Simulations: A Lake-ICE Project

UW 144-GW37
NSF ATM-9707165

E.W.Eloranta
Principal Investigator

University of Wisconsin
Space Science and Engineering Center
1225 W. Dayton St.
Madison, WI
Tel (608)-262-7327

November 12, 1999

Introduction

During the second year of this grant our efforts have included:

- Lidar wind measurements

  Extended existing wind algorithms to provide spatially resolved winds.

  Developed algorithms to compute divergence from lidar winds.

  Developed algorithms to compute vorticity from lidar winds.

  Processed wind data for Jan 10 and Jan 13 Lake-ICE lidar data.

- Large-eddy simulations (LES)

  Compared UW-NMS LES predictions with results from other LES models.

  Generated realistic inflow profiles using radiosonde data and LES model runs.

  Tested use of random perturbations in the upwind velocity field to initiate instability.

  Modeled January 13, Lake-ICE case with a 6 km fetch upwind of the shoreline.

This report provides a brief description of these activities along with a list of conference papers and copies extended abstracts written for these conferences.

Wind Measurement Algorithms

In previous work we have developed algorithms to measure vertical profiles of the horizontal wind from volumetric lidar images of aerosol structure (Schols and Eloranta 1992, Piironen and Eloranta, 1995). These algorithms derived a single wind vector for each altitude representing the mean wind averaged over the ~ 100 km^2 area of a typical lidar scan.

Wind processing for the lake-ICE data follows the basic approach described in our previous papers except that a spatially resolved grid of wind vectors is derived from a series of lidar scans showing a single horizontal plane . The initial processing proceeds as follows:

1. Individual lidar shots are corrected for the r^{-2} dependence in lidar equation and then filtered with a running median hi-pass filter. The filter length was set to 450 m for the results presented in this report.

2. Next the lidar data is mapped to a Cartesian grid with a uniform spatial resolution of 15 meters. Data points on the Cartesian grid are computed from a linear interpolation between the 4 nearest points in the polar coordinates of the raw lidar profiles. To correct for the distortion of the lidar image caused by the wind, and a finite scan duration, the position of data points in the lidar profiles are adjusted to the location they occupied at the time the first profile of the scan was acquired. The wind vector needed for this adjustment are found by applying the solution iteratively.

3. A temporal-median image is then formed from the complete set of Cartesian scan images. This median image is subtracted from each of the scan images prior to further processing in order to remove station features and artifacts caused by attenuation.

4. Finally, to prevent individual bright features in the image from dominating the cross correlation function, the resulting images are subjected to a histogram normalization.

Up to this point the wind processing is nearly identical to the scheme for computing winds averaged over the entire scan area as described in Piironen and Eloranta. However, in order to compute the spatial variation of the wind field, the scan area must now be divided into smaller sub-areas. Two-dimensional lag cross correlations are computed between successive scans in each of the sub-areas. These cross correlation functions are then averaged over a series of scan pairs. Wind vectors are then computed from the lag positions of averaged correlation function maximums and the time separation between scans.

In the computations presented below, winds are calculated in square sub-areas which are 250 meters on a side. Correlations are computed between every other scan so that left-right/right-left scans are always paired with the same scan direction and thus the time interval between laser profiles in each part of successive images is approximately the same. This results in a $\sim$ 24 sec time separation between scans. Because the winds were as large as 9 m/s, the wind advected aerosol structures by up to 216 meters between scans. This causes a problem with the wind calculation because most of the structure seen in a sub-area in one scan has advected out of the sub-area by the time of the next scan. This creates small correlation maxima contaminated by random correlations between unrelated structures. To minimize this problem the correlation calculation is modified. The location of the sub-area in the second frame of each pair is displaced downwind by the distance the structure is expected to move between frames. This allows the correlation to take place with approximately the same features that were present in the first frame. The position of the correlation maximum is then corrected for the displacement of the box to compute the wind vector. An estimate of the wind vector is required in order to select the displacement for the sub-area in the second frame. This is computed by first generating a lower resolution wind field where the advection distance is a smaller fraction of the sub-area's size. For the winds shown below, the wind field was first calculated in square sub-areas with sides of 500 m. The 500 m values were then used to compute displacements for the four 250 m areas in each of the larger areas.

Data from January 10, 1998

Figure 1 shows the average wind field computed for data acquired between 14:16 and 14:57 UT on Jan 10, 1998. The wind shadow in the lee of the coastline is clearly visible. The wind shadow length varies with north-south position. This probably reflects variations in the topography and surface roughness along the shore. The acceleration and veering of the wind as it leaves the shore is clearly seen in figure 8. This presents a north-south average of the wind speeds and directions along with a crude estimate of errors. The length of the error bars were computed from the variance of the values contributing to each north-south

average. The plotted length of the error bar is equal to the variance divided by the square root of the number of points ($\sqrt{24}$ in this case) contributing to the average. While these error bars provide an estimated upper bound for the random fluctuations in the wind, they are not true error estimates. They tend to underestimate the true error by failing to include systematic errors while at the same time tending to overestimate the errors because the true geophysical variability is included in the calculated variance.

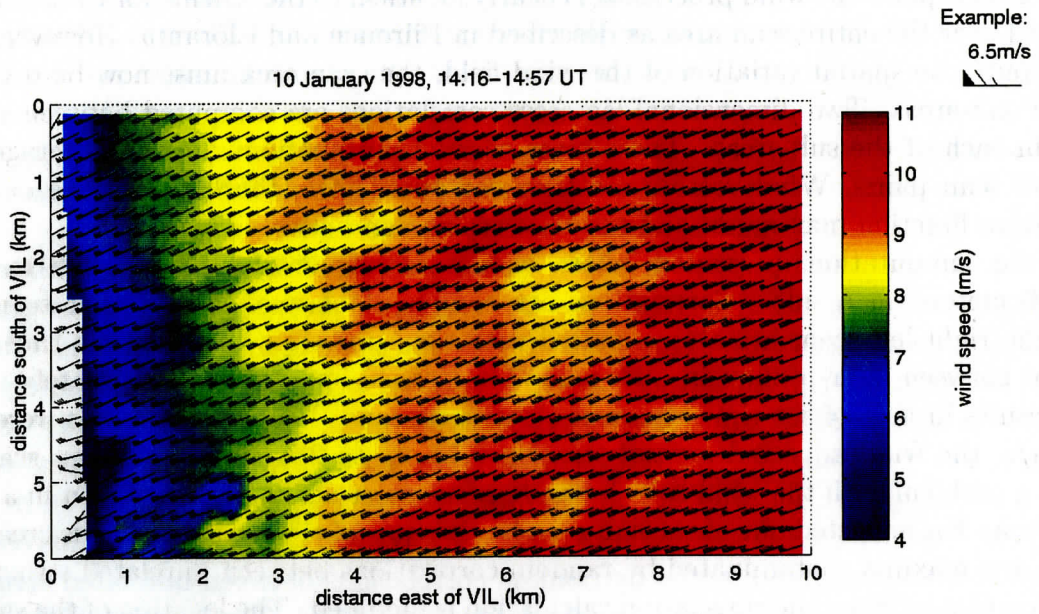

Figure 1. Wind vectors computed from 240 PPI scans acquired between and CST on January 10, 1998. Meteorological wind barbs are presented with single barbs indicating 1 m/s. Wind barbs are plotted at the centers of the first sub-area used in the correlation computation. At the edges of the scan where the sub-area are not completely covered by the lidar scan, the vectors are plotted at the center of gravity of the scanned area. Vectors are not plotted if less than 25% of the sub-area was covered by the lidar scan.

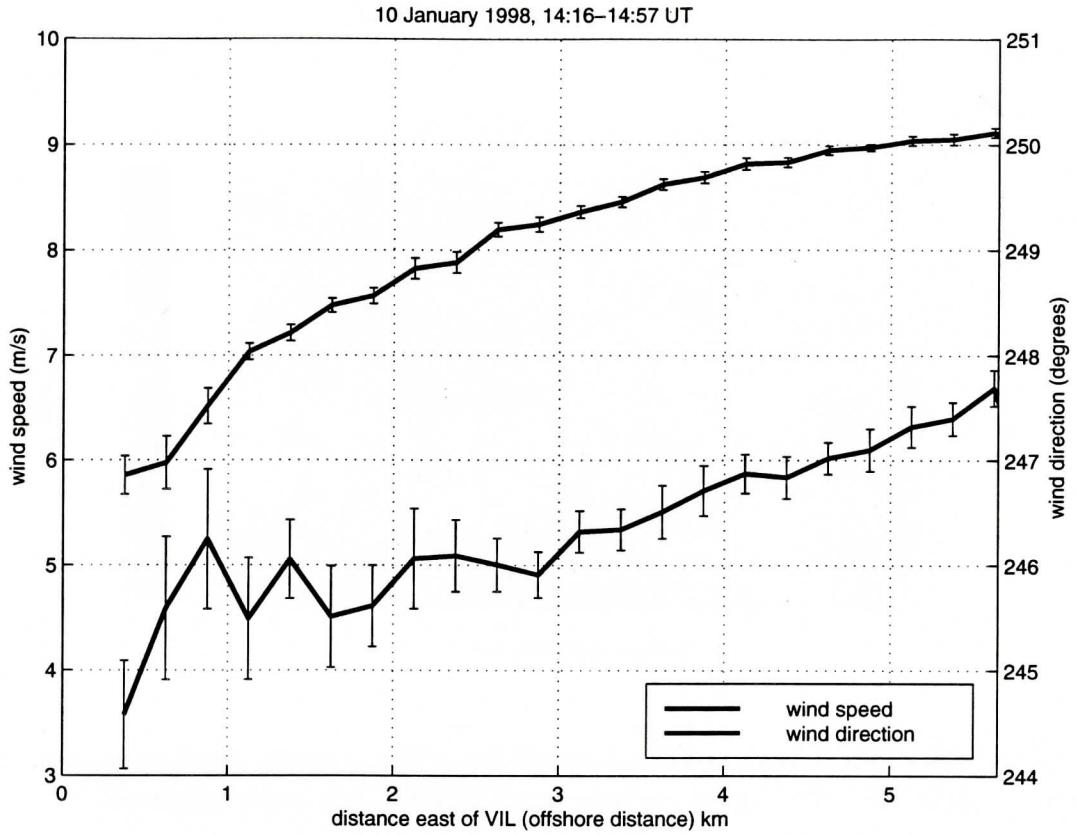

Figure 2. Average wind speed and direction as a function of distance from the shore between 14:15 and 14:57 UT on January 10, 1998. The acceleration and veering of the wind with offshore distance are clearly seen. This plot is computed from a north-south averaging of the data shown in figure 6. Only those vectors computed from areas completely covered by the lidar scan are used in the average.

Figure 3 shows the divergence field computed from the wind data in figure 1. Notice the strong divergence along the shoreline caused by the acceleration of the wind as it adjusts to the lower surface roughness lengths presented by the water relative to the land. A narrow band of divergence extends downwind from a point $\sim$ 3.2 km south of the lidar. The Edgewood power plant, which consists of a very large building complex, is located at this point on the shore and it appears as if this divergence feature may represent a building wake or possibly an artifact caused by the slow meandering of the weak surface aerosol plume emitted by the power plant. This is one of many intriguing observations which must be investigated carefully in our continuing data analysis.

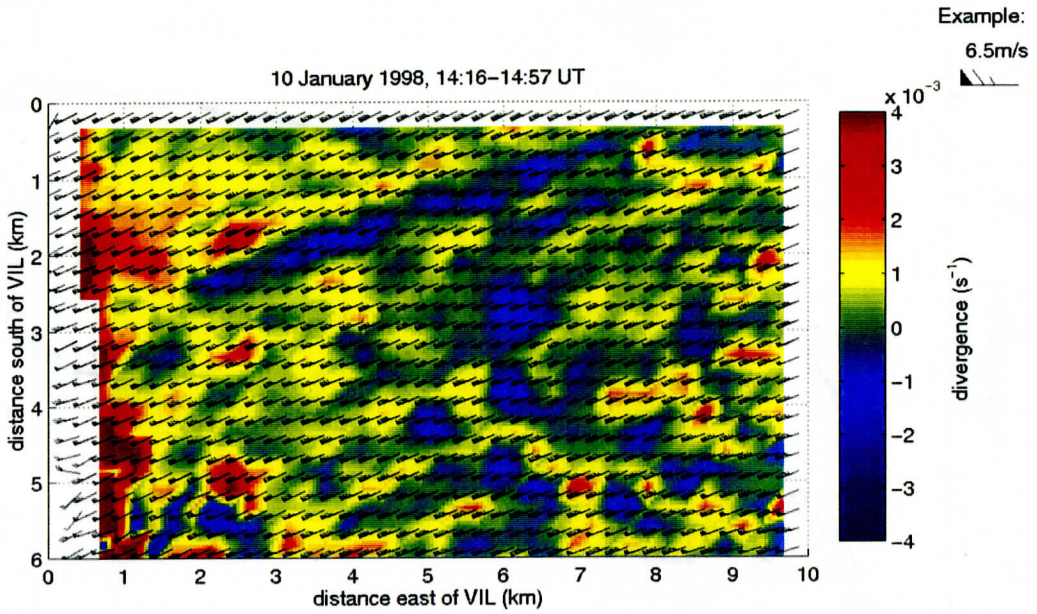

Figure 3. The divergence field computed from the velocity field presented in figure 7 is shown in colors. The wind vectors from figure 1 are superimposed.

Figure 4 presents the divergence as a function of distance from shore calculated from the data presented in figure 9. Random variations in the smoothed curve between 3.5 and 5.5 km from shore appear to be less than 10^{-4} s^{-1}. This is an encouraging result, since these results are expected to improve as the wind algorithms are optimized for this application.

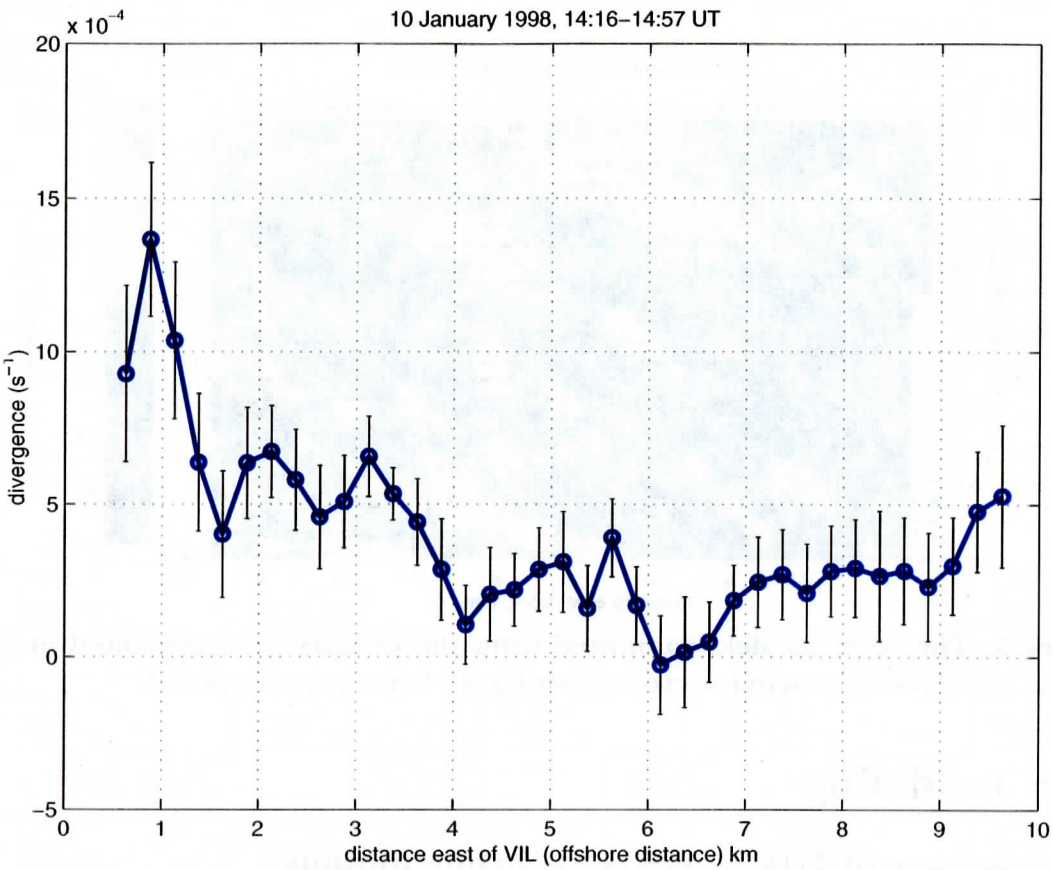

Figure 4. Divergence as a function of distance from the shore between 14:15 and 14:57 UT on January 10, 1998. The plotted points are the divergence values computed directly from the data presented in figure 1.

Figure 5 shows the vorticity field computed from the wind field shown in figure 1. Strong negative vorticity appears along the shoreline as the wind veers in response to the smaller friction over water. Here, the possible wake feature shown in the divergence field appears as a strong negative vorticity wake. At distances greater than ~ 3 km from the shore there is evidence of a coupled band of positive vorticity north of the negative band.

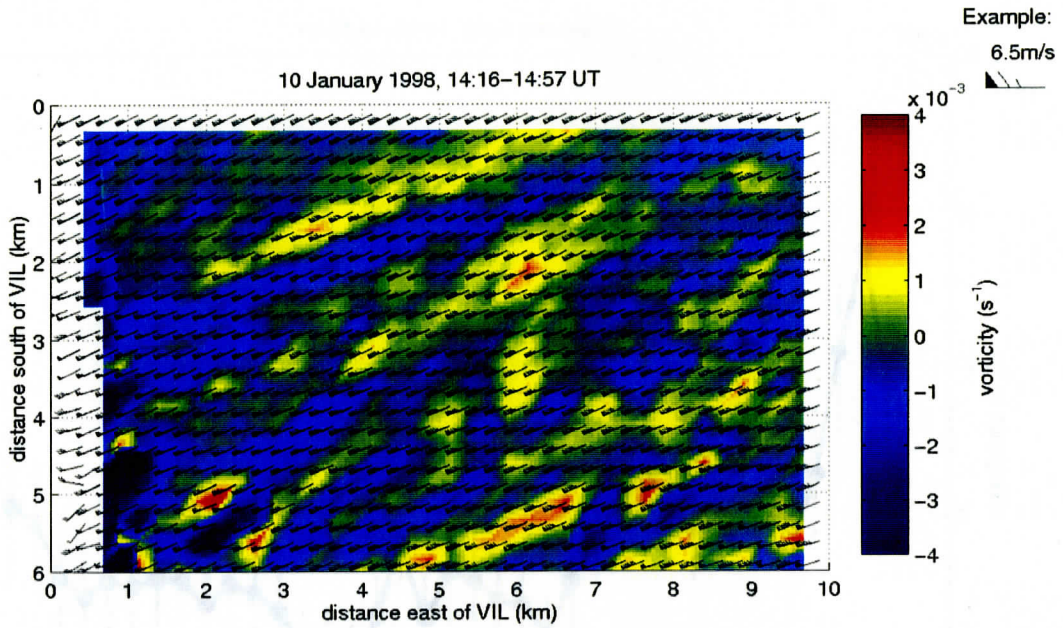

Figure 5. The vorticity field computed from the velocity field presented in figure 7 is shown in colors. The wind vectors from figure 7 are superimposed.

LES modeling

Comparison of UW-NMS with other models

Nieuwstadt et al. (1993) have modeled a single clear air convective boundary layer situation with Large Eddy Simulation models from several different research groups. As a first test of the UW-NMS code in LES mode, we have generated predictions for the same conditions.

This simulation utilized a model domain of 40 x 40 x 60 grid-points that was 6.4 km x 6.4 km wide (160 m horizontal resolution) and 3-km tall (50 m vertical resolution). We supplied 0.06 K m/s sensible heat-flux at the surface and turned off radiation and the soil model in UW-NMS. This case contains no moisture and is initialized with a neutral sounding from the surface to an altitude of 1500 m. All parameters match those of Nieuwstadt et al. The temperature and w-component of velocity are randomly modulated at the beginning of the simulation to help speed to development of large-eddies. The time-step for this simulation was 5 s.

The UW-NMS provides predictions similar to the results published by Neuwstadt et al. For example, figure 6 shows vertical profiles of vertical velocity variance normalized by the convective scaling velocity w_*.

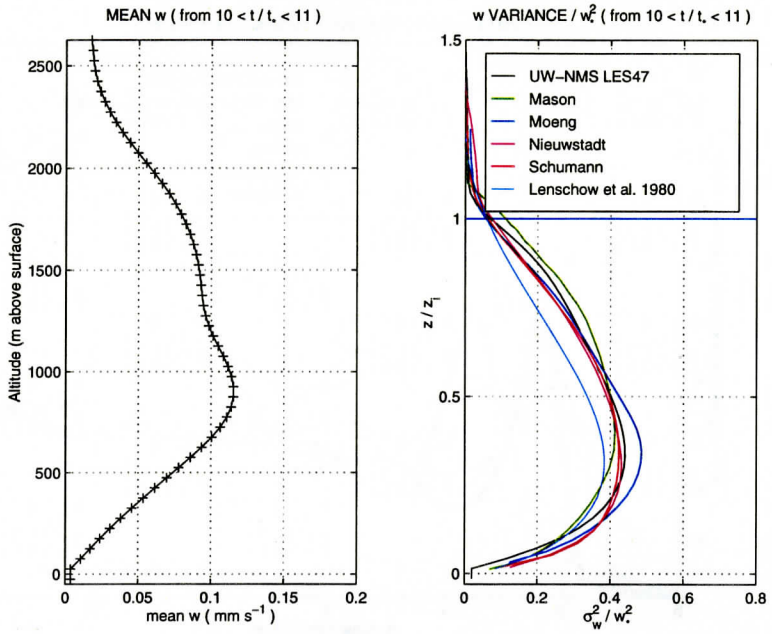

Figure 6. Mean vertical velocity(left) and a comparison of normalized vertical velocity variance derived from the UW-NMS and other LES models (right).

Figure 7 provides a comparison of the total kinetic energy in the model domain as a function of dimensionless time. Here, $t_* = 1096$ s. Once again the UW-NMS results are very similar to those shown by Neuwstadt. A sharp increase and overshoot in the total-TKE occurs for all the codes between $2 < t/t_* < 4$. This corresponds to the period between 36 and 73 minutes after initialization. This burst of convective activity illuminates a problem with the assumptions used in LES modeling; the approach does not provide a mechanism for instabilities to grow from subgrid scales to the resolved scales. This delays the formation of convective elements and allows the buildup of a unrealistically intense super-adiabatic surface layer before the convective burst.

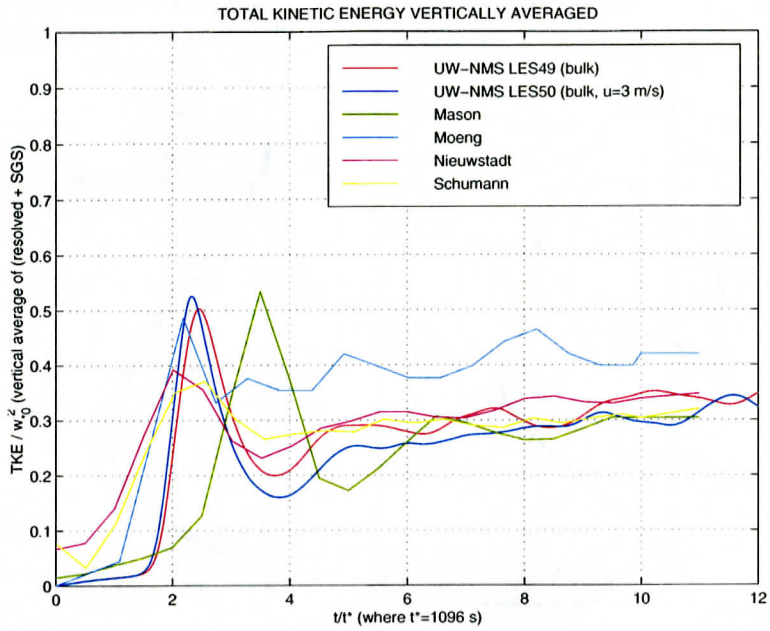

Figure 7. Total-TKE as a function of time in the simulation of a convective boundary layer for several codes including the UW-NMS.

Initial attempts to model the developing convective boundary layer over Lake Michigan also showed this delay in the development of convection. These solutions showed a laminar flow region extending some distance over the lake followed by a band of unrealistically vigorous convection. To avoid this we have found it necessary to supply small random point to point velocity variations near the surface close to the inflow boundary. These perturbations produce velocity gradients in the resolved scale which initiate the growth of organized mixed layer circulations much earlier than in the non-perturbed case.

We had expected to encounter a very shallow shear driven turbulent boundary layer under a nearly laminar flow at the lake edge. Contrary to expectation, our lidar and radiosonde data shows that the inflow flow layer is mixed and contains organized structures all the way up to a capping inversion at an altitude of approximately 400 m. This makes it much more difficult to specify the upwind boundary condition because an accurate simulation requires fully formed turbulent structures at the lake edge.

In attempt to provide the observed structure at the lake edge we have expanded our model domain to include a 6 km fetch upwind of the lake. The inflow at the upwind boundary is specified with a profile generated from the radiosonde and a LES model run which supplies realistic profiles in the surface layer. A random resolved scale velocity perturbation with a maximum variation ± 0.5 cm/sec is applied to the the bottom 45 m of the profile at 500 m from the upwind wall. This provides velocity gradients which speed the evolution of large scale turbulent structures in the remaining distance to the lake. These simulations use a constant grid spacing of 15 m and cover a total area 12 km in the east-west direction, 1.65 km in the north-south direction and 1.025 km in the vertical. Figure 8 provides an example of the vertical velocity field computed at 7.5 m above the surface after 30 min of simulation

using time steps of 0.5 s.

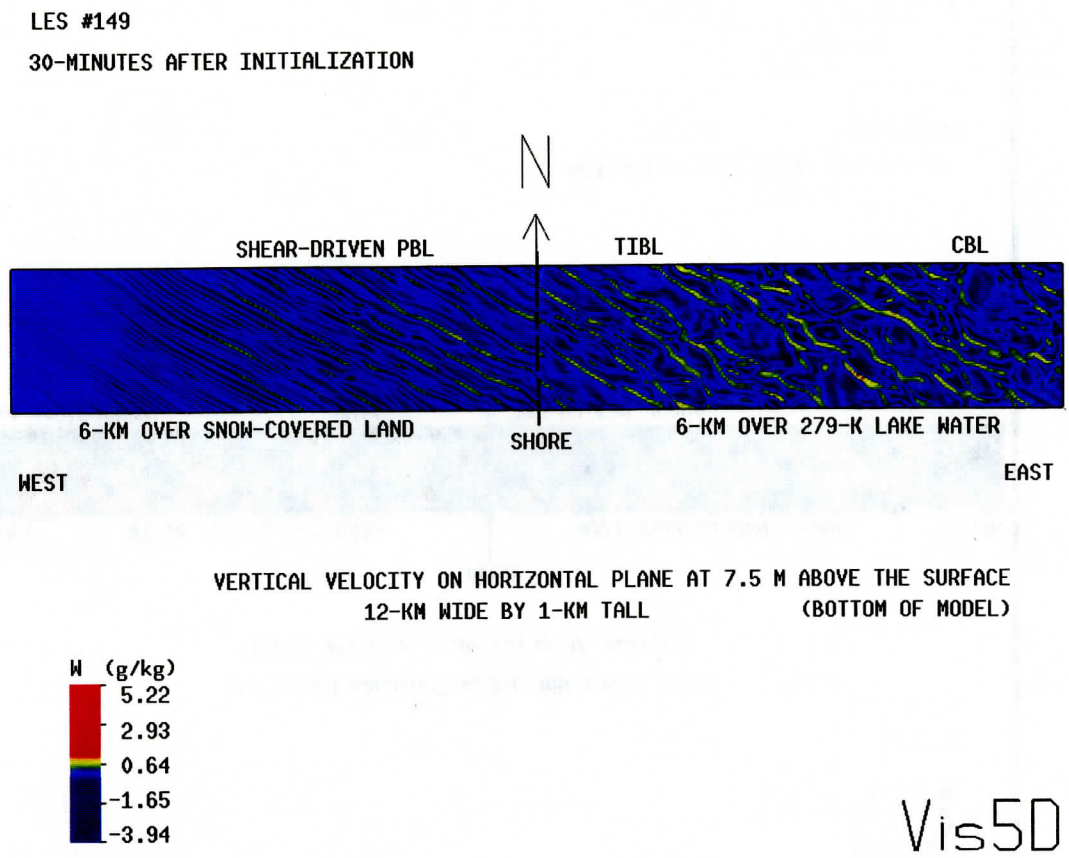

Figure 8. Vertical velocity at an altitude of 7.5 m after 30 minutes of simulation.

This figure shows the formation, growth and merging of longitudinal roll circulations, beginning at the west (inflow) boundary and continuing up to the shore line. Downwind of the shore the rolls slowly evolve into cellular structures similar to those seen in the lidar scans.

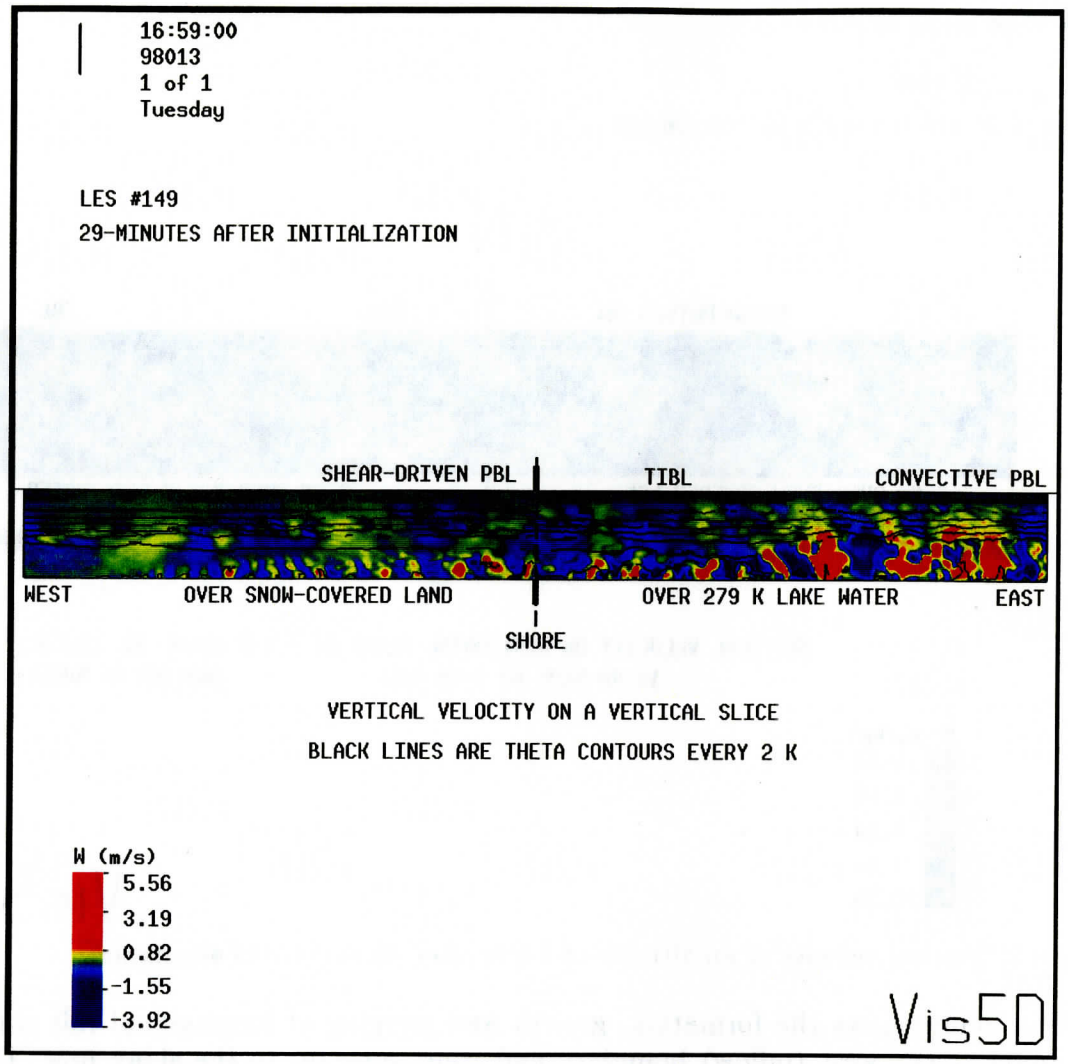

Figure 9. Vertical velocity on vertical slice after 29 min of simulation.

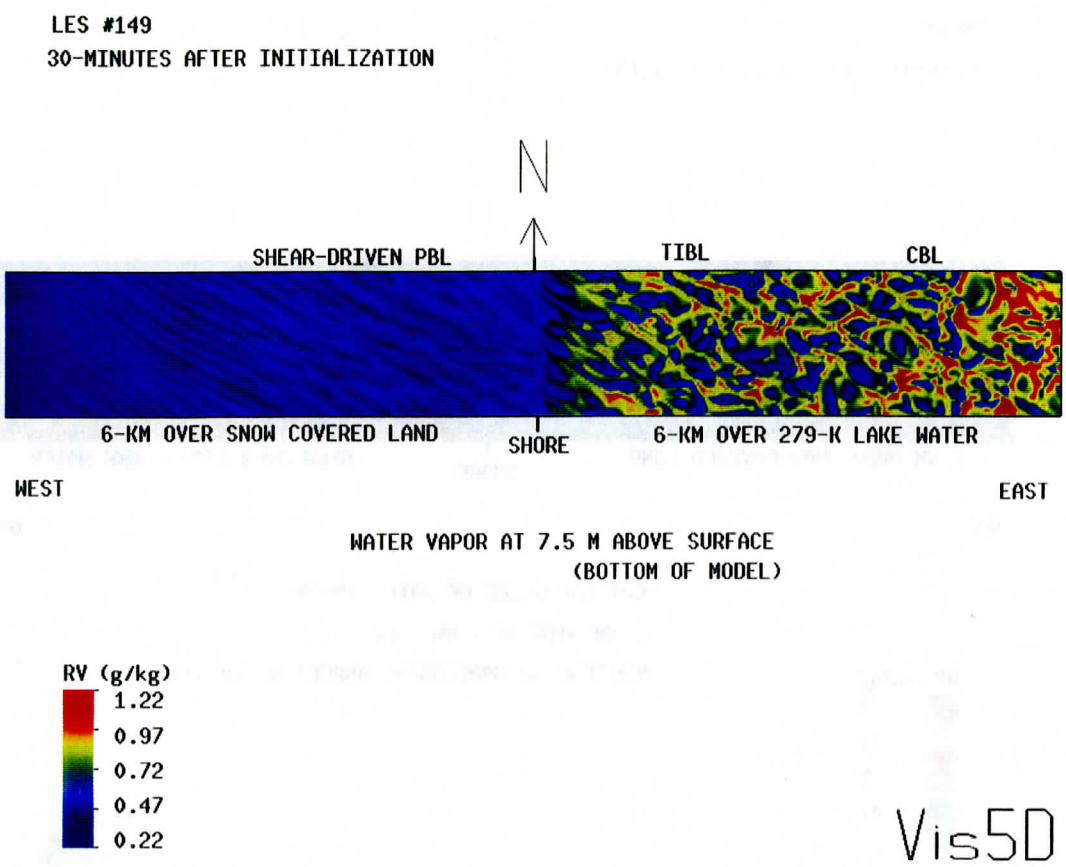

Figure 10. Water vapor at an altitude of 7.5 m after 30 minutes of simulation.

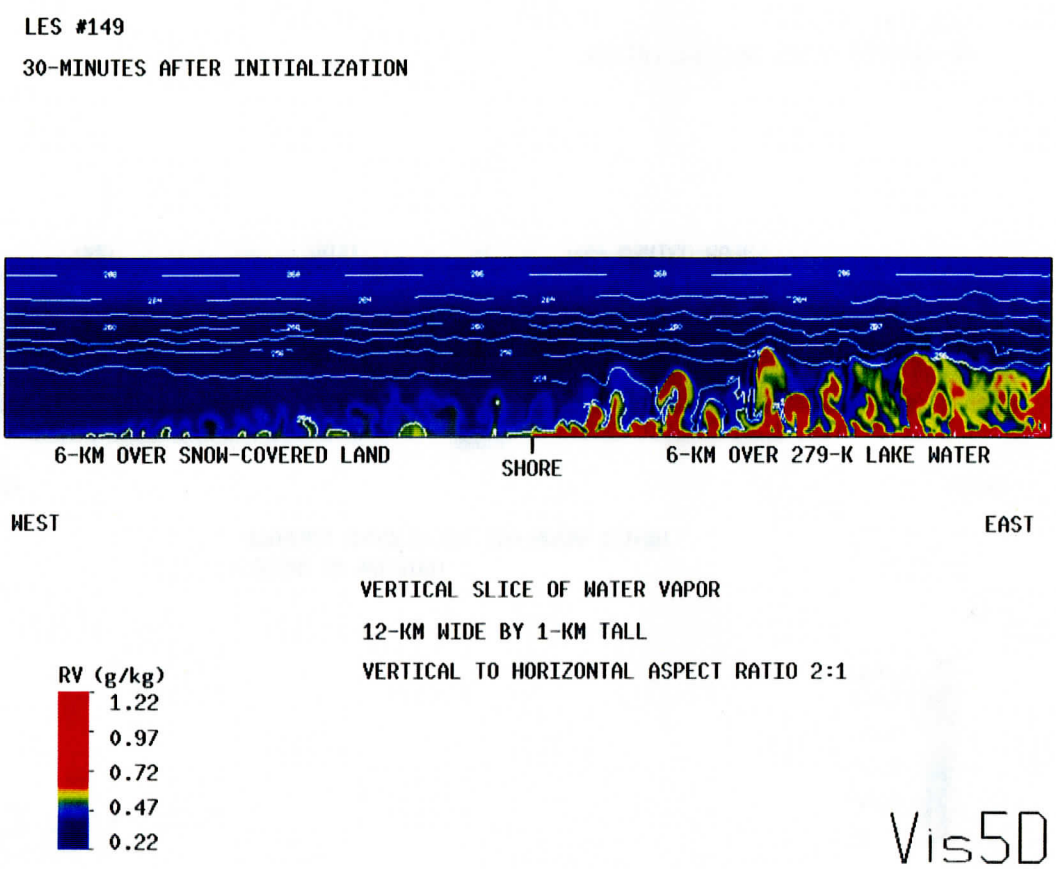

Figure 11. Water vapor (colors) and potential temperature (contours) as a function of altitude and west-east distance after 30 minutes of simulation. Water vapor plumes upwind of shore line are produced by sublimation from snow surface.

Conference Presentations

Our Lake-ICE work has been presented in a total of six conference papers. A poster presented by Shane Mayor et al, describing our Lake-ICE work, at American Meteorological Society Conference on Boundary Layers and Turbulence was award a second place prize for best student poster of the meeting. Abstracts of papers not included in last years report are appended to this report.

- Eloranta, E. W., S. D. Mayor and J. P. Garcia, *Lidar Measurements of Vector Wind Fields*, The Pacific Rim Convergence on Lasers and Electro-Optics, Aug 30-Sept 3, 1999, Seoul, Korea.

- Eloranta, E. W., S. D. Mayor and J. P Garcia, *Measurements of Wind, Divergence, and Vorticity Fields with the University of Wisconsin Volume Imaging Lidar*, Optical Society of America Topical Meeting on Optical Remote Sensing of the Atmosphere, June 21-25, Santa Barbra, CA.

- Mayor, S. D., G. J. Tripoli, E. W. Eloranta, and B. D. Hoggart, *Preliminary comparison of Lake-ICE volume imaging lidar data and large eddy simulations,* American Meteorological Society Conference on Boundary Layers and Turbulence, Jan 1999, Dallas, TX.

- Eloranta, E. W., R. E. Kuehn, S. D. Mayor, and P. Ponsardin, *Near-Shore Boundary Layer Structure of Lake Michigan in Winter*, American Meteorological Society Conference on Boundary Layers and Turbulence, Jan 1999, Dallas, TX.

- Eloranta, E. W., S. D. Mayor, R. Kuehn, P. Ponsardin and J. Hedrick, *Volume Imaging lidar observations of atmospheric boundary layer structure over the western edge of Lake Michigan*, 4th-International Symposium on Tropospheric Profiling, Sept 20-25, 1998, Snowmass, CO.

- Eloranta, E., R. Kuehn and S. Mayor, *Lidar Observations of a Land-Breeze Circulation*, 19th-International Laser Radar Conference, July 6-10, 1998, Annapolis, MD.

References

- Nieuwstadt R. T. M., P. J. Mason, C-H. Moeng, and U. Schumann, 1993: Large-eddy simulation of the convective boundary layer: a comparison of four computer codes. *Turbulent Shear Flows 8.* 343-367, Eds. F. Durst et. al., Springer-Verlag, Berlin.

- Schols, J. L., and E. W. Eloranta, 1992: The calculation of area-averaged vertical profiles of the horizontal wind velocity from volume imaging lidar data ., *J. of Geophys. Res.*, **97**, 18395-18407.

- Piironen, A. and E. W. Eloranta, 1995: An accuracy analysis of the wind profiles calculated from Volume Imaging Lidar data, *J. of Geophys. Res.*, **100**, 25559-25567.

Presented at the Conference on Lasers and Electro-Optics
Aug 30-Sept 3, 1999, Seoul, Korea.

Lidar Measurements of Vector Wind Fields

E. W. Eloranta, S. D. Mayor, and J. P. Garcia
University of Wisconsin-Madison
Madison, WI 53706
tel: 608-262-7327, fax 608-262-5974
eloranta@lidar.ssec.wisc.edu

Introduction

In this paper, both horizontal components of the wind vector are measured with 250 m spatial resolution over a 6 by 10 km area. These are derived using 2-dimensional cross-correlations computed between a series of aerosol backscatter images recorded with the University of Wisconsin Volume Imaging Lidar (VIL).

The VIL is designed to provide high spatial and temporal resolution images of atmospheric structure. It employs a 1.06μm laser operating at a repetition rate of 100 Hz, 0.5-m diameter scanning optics, and a fast data acquisition system to generate two- and three-dimensional images. Under typical conditions, the system records data to a range of 18 km with a range resolution of 15 m. The data system records profiles without averaging. Approximately 1 G-byte of data is recorded per hour of operation.

This paper analyzes repeated azimuthal scans made with the lidar elevation angle set near zero. A typical scan covered an azimuthal sector of $\sim 100°$ and provided lidar profiles at $\sim 0.08°$ increments. The full back-and-forth scan was repeated at ~ 25 s intervals.

Wind Calculations

We have previously developed algorithms to measure vertical profiles of the horizontal wind from a series of volumetric lidar images of aerosol structure (Schols and Eloranta 1992, Piironen and Eloranta, 1995). These provide a single wind vector for each altitude representing the mean wind averaged over the ~ 100 km^2 area of a typical scan. In this paper, these algorithms are modified to provide a vector wind field with a 250 m spatial resolution. Correlations are computed between square image segments which are 250 meters on a side. Correlations are computed between every other scan so that left-moving and right-moving scans are always paired with the same scan direction and thus the time interval between laser profiles in each part of successive images is ~ 25 s. Because the winds were as large as 9 m/s, the wind advected aerosol structures by up to 225 m between scans. This created noise in the cross correlation calculation because most of the structure seen in the first image

was advected out of the image area before the next scan. To minimize this problem, the second image in each correlation pair is selected from a position displaced downwind of the first image by the distance the structure is expected to move between scans. This allows the correlation to take place with approximately the same air mass that was present in the first image. The displacement of the image position is added to the displacement of the correlation peak to compute the wind vector. The a priori wind vector required to compute the displacement of the second image is computed by first generating a wind field with 500 m spatial resolution where the advection distance is a smaller fraction of the image size.

Figure 1 shows the wind field computed from data acquired 5 m above the surface of Lake Michigan as cold air ($-20°$ C) passed over 6° C water. Figure 2, which presents North-South averages, shows the acceleration and veering of the wind as it leaves the shore. The wind shadow in the lee of the coastline is clearly visible. A careful examination of figure 1 shows that the wind shadow length varies with position. This reflects variations in the topography and surface roughness along the shore. The error bars in figure 2 were computed from the variance of the values contributing to each north-south average; with the errors set equal to the square-root of the variance divided by the square root of the number of points contributing to the average (24 points in this case). These tend to underestimate the true error by failing to include systematic errors while at the same time tending to overestimate the errors because the true geophysical variability is included in the calculated variance. The estimated errors in the North-South average wind speed and direction are $\sim$ 10 cm/s and $\sim 0.5°$ respectively, while for the individual wind measurements shown in figure 1, the estimated errors are $\sim$ 50 cm/s and 2.5° for the speed and velocity respectively.

This paper will also present divergence and vorticity fields computed from the vector winds.

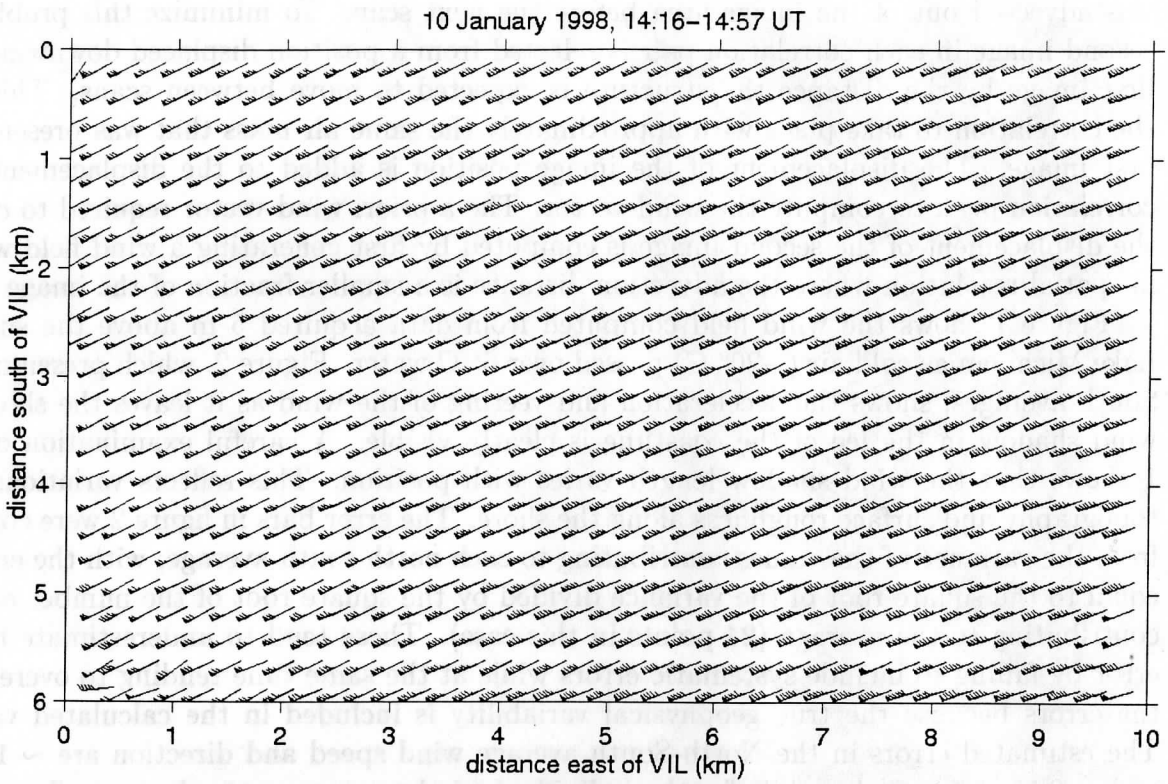

Figure 1. Wind vectors computed from 240 PPI scans 5 m above lake Michigan during a cold air outbreak between 14:15 and 14:57 UT on January 10, 1998. The shore line roughly parallels the left edge of the figure. Meteorological wind barbs are presented with single barbs and triangles indicating 1 m/s and 5 m/s respectively.

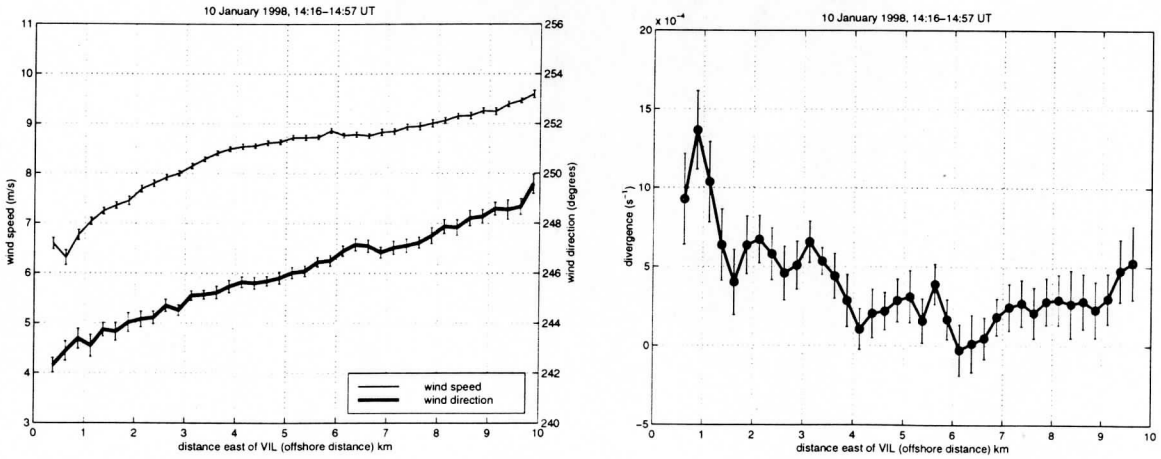

Figure 2. Average wind speed, direction (left-panel) and divergence (right-panel) as a function of distance from the shore between 14:15 and 14:57 UT on January 10, 1998. The acceleration and veering of the wind with offshore distance are clearly seen. This plot is computed from a north-south averaging of the data shown in figure 1.

References

- Schols, J. L., and E. W. Eloranta, 1992: The calculation of area-averaged vertical profiles of the horizontal wind velocity from volume imaging lidar data ., *J. of Geophys. Res.*, **97**, 18395-18407.

- Piironen, A. and E. W. Eloranta, 1995: An accuracy analysis of the wind profiles calculated from Volume Imaging Lidar data, *J. of Geophys. Res.*, **100**, 25559-25567.

Presented at the American Meteorological Society Conference on Turbulence and Diffusion
Jan, 1999, Dallas, TX

Near-Shore Boundary Layer Structure over Lake Michigan in Winter

Edwin W. Eloranta, Ralph E. Kuehn, Shane D. Mayor and Patrick Ponsardin
University of Wisconsin-Madison
1225 W. Dayton St., Madison, Wisconsin, 53706, USA
phone: 608-262-7327, fax: 608-262-5974, e-mail: eloranta@lidar.ssec.wisc. edu

Introduction

The wintertime flow of cold air over warm water produces a vigorous growing convective boundary layer along the upwind shore of Lake Michigan. This boundary layer, which increases in depth with distance from the upwind shore, provides an attractive setting in which to observe the development of convective structures. The water surface provides a lower boundary with nearly uniform temperature and flat topography to facilitate model calculations.

This paper presents observations gathered by the University of Wisconsin Volume Imaging Lidar (VIL). The lidar was deployed on the lake shore at Sheboygan, WI, as part of the Lake Induced Convection Experiment (Lake-ICE). The lidar observations were designed to provide data to test Large Eddy Simulation models. Data were acquired on 9 days between December 5, 1997 and Jan 22, 1998. Supplementary local data were collected by an NCAR integrated sounding system (ISS) located 10-km west of the lidar and by the National Data Buoy Center's SGNW3 weather station located 3/4-km north of the lidar.

Figure 1. The lidar was located on the West shore of Lake Michigan at Sheybogan.

Convective structures

A variety of convective structures were observed during periods when cold air advected over the warm water. Of particular interest are images showing open cells with downward motion in the center, upward motion in narrow cell walls, and approximately hexagonal cross sections. These were observed on both January 10th and 13th. An image of these cells observed on Jan 10th is shown in figure 2.

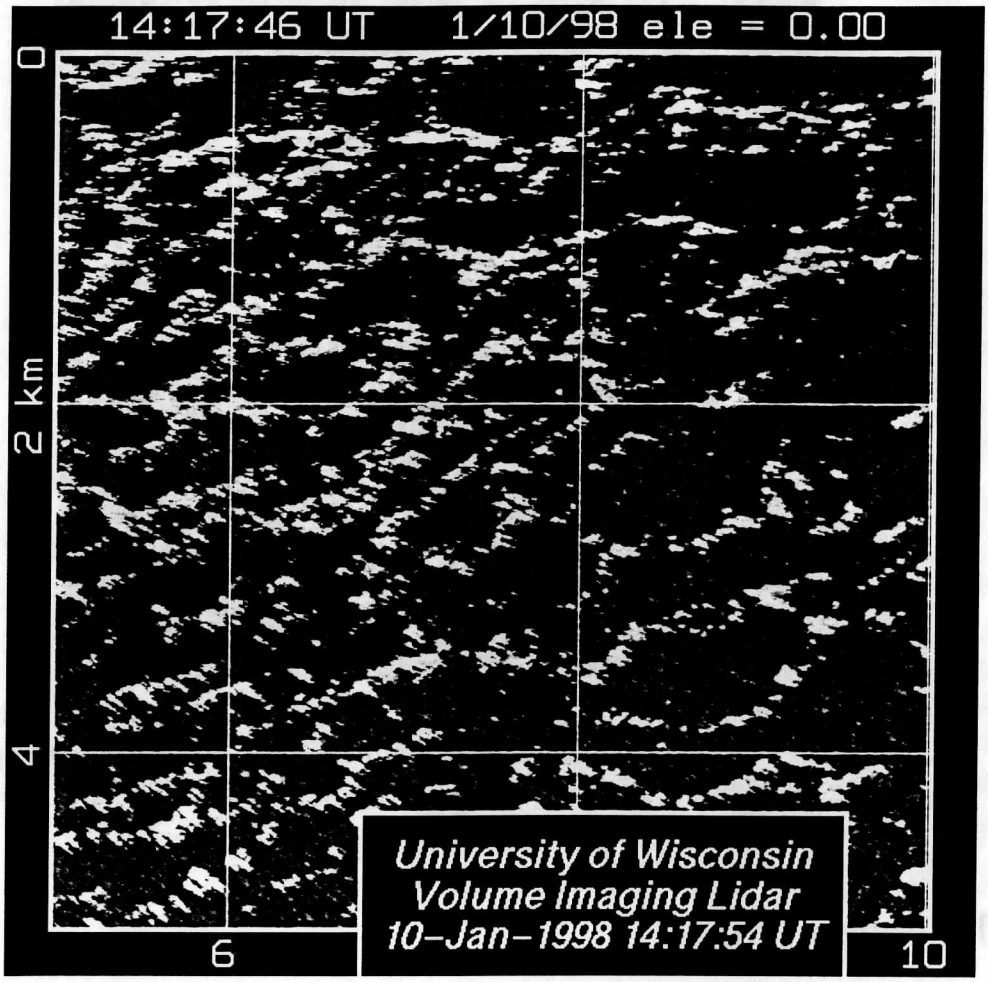

Figure 2. Enlargement of a 25-km^2 region 5-10 km offshore from a PPI image of range-corrected backscatter intensity. The image shows open-cell organization of convection in the steam-fog over the lake during a cold air outbreak on 10 January 1998. Note the approximately hexagonal shape of the cells. At the shore, the mean wind during this time was from 236° at 6.5 m s^{-1} and the air temperature was -16.7° C.

Lidar volume scans obtained on January 13 showed narrow columns of steam-fog rising nearly to the the top of the mixed layer at $\sim$ 400 meters. Steam-devils were observed visually during this period. Large eddy simulations of the flow field for this day are presented in a separate paper (Mayor et al.) at this conference.

Closed cells with upward vertical motion in the center were observed on January 19. Figure 3 shows a azimuthal scan obtained at an elevation angle of 1.5°. Bright echos are seen at a range of $\sim$ 9 km where the lidar beam hits the bottoms of clouds at at an altitude of $\sim$ 250 m. At 16 UTC the Coast Guard station reported a temperature of $-4.1°$ C with a wind of 2 m/s from a direction of 300°.

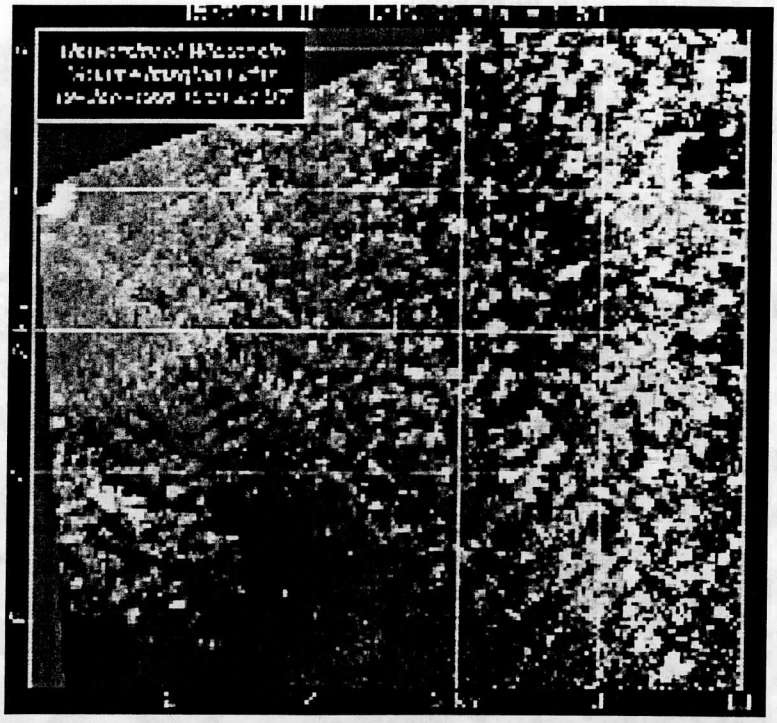

Figure 3. Closed cell convection observed at 15:01 UTC on January 19, 1998. An area of 10 by 9 km is shown. The lake shore is located approximately along the left edge of the the image. At the lidar the beam is $\sim$ 5 m above the lake surface. The 1.5° elevation angle increases the altitude to 255 m at a range of 9 km.

Land-breeze front

Vivid images of a land-breeze front and its temporal evolution were recorded on December 21, 1997. A large high-pressure system centered northeast of Lake Huron moved slowly eastward during the observation period. The resulting pressure gradient supported a weak southeasterly (on shore) synoptic flow. Figure 4 shows the wind speed and direction measured at the Coast Guard station.

The morning low temperature at the Sheboygan airport ($\sim$ 10 km inland from the lidar) was $-6°$ C and it occurred at 14:00 UTC. The airport temperature rose slowly to $-1°$ C by 17:00 UTC. The morning low temperature at the Sheboygan Coast Guard station (3/4 km north of the lidar on the shore line) was $-3.4°$ C at 11 UTC and the temperature rose to 1.6° C at 18 UTC. NOAA-satellite derived temperatures for the water offshore from the

lidar were between 4° and 5° C.

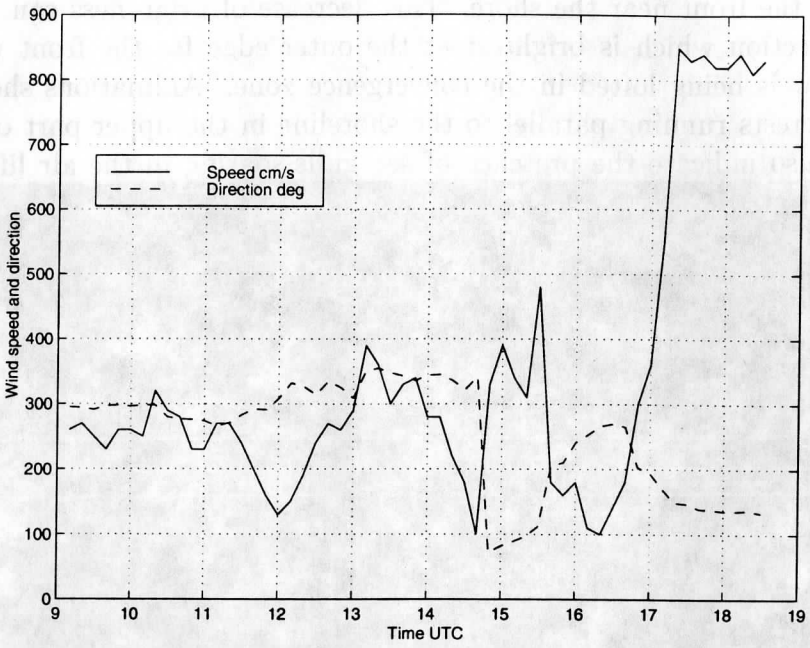

Figure 4. Wind speed and direction measured at the Sheboygan Coast Guard station between 9:00 and 18:30 UTC. The Coast Guard station is located 3/4-km North of the lidar site. Notice that the land-breeze front breaks down at 17:00 UTC under the influence of a weakening land-water temperature differential.

The lidar recorded volume scans between 13:12 UTC and 15:21 UTC. Each volume scan provided 101 separate RHI scans ($0 - 15°$ elevation) in the azimuth range between 126° and 176°. The volume scan was repeated at intervals of 187 seconds. Figure 5 shows a sample image derived from one of these scans. This image includes one RHI scan along with two constant-altitude cross section created from the same volume scan. Due to the small format available in these proceedings, the horizontal cross sections are enlarged to show only a small portion of the 12-km north-south extent of the lidar images.

The RHI image shows that the front decreases in depth with distance from the shore. It also shows the thin bright land-breeze outflow layer within $\sim$ 20 m of the surface; this

is the cold layer of air sliding out over the water against the synoptic flow. Animation of the RHI cross section shows that the land-breeze outflow is confined to a thin layer near the surface. This air appears to flow along the surface to the front where it rises in a strong convergence zone and is then swept back inland in the layer above the outflow. This return flow appears to undergo strong mixing with the marine boundary layer as it is forced up over the land-breeze front. This mixing is evident in the decreased brightness of the upper part of the front near the shore. This decrease of brightness can also be seen in the 110-m cross section which is brightest at the outer edge for the front where air from the surface outflow is being lofted in the convergence zone. Animations show the presence of gravity-wave crests running parallel to the shoreline in the upper part of the front. Point-target-echos also indicate the presence of sea gulls soaring in the air lifted over the front.

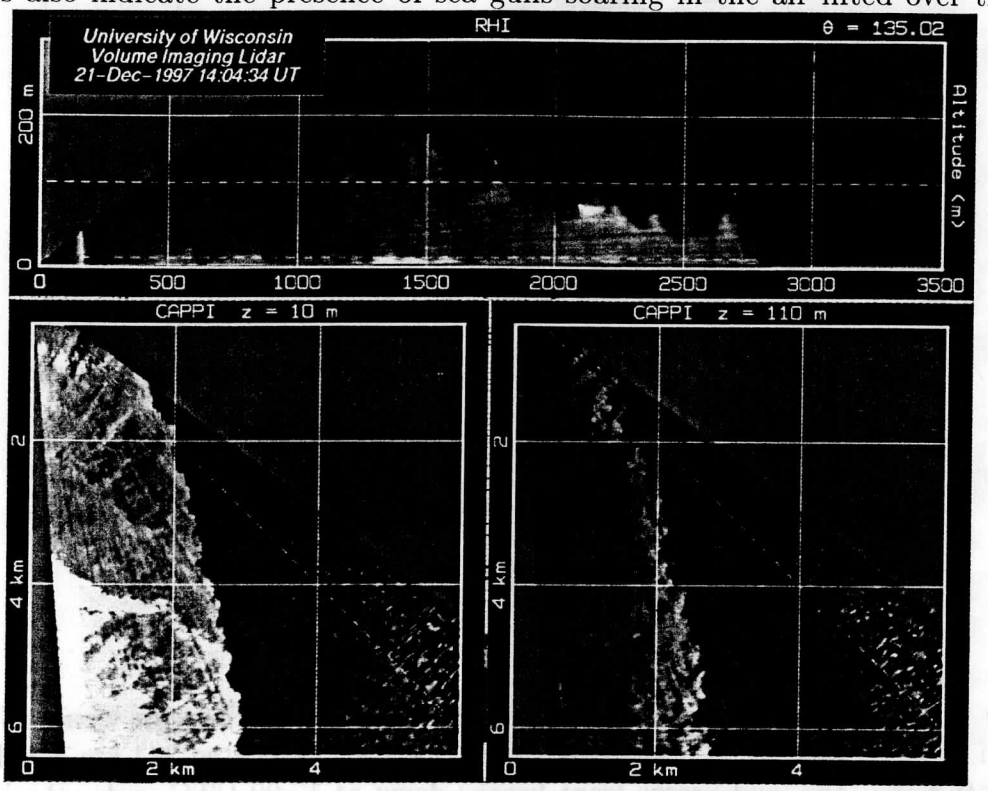

Figure 5. The land-breeze front observed at 14:04 UTC on December 21, 1997. The top panel shows a RHI cross section extending from the surface to an altitude of 300 m and a maximum horizontal range of 3500 m. The RHI is oriented at a compass heading of 134 degrees. The bottom panels show horizontal cross sections over a 6- by 6-km square area at altitudes of 10 m (left) and 110 m (right). North is at the top of the horizontal cross sections and the shoreline runs roughly along the left edge of the images.

The 10-m constant altitude scan shows the cold aerosol laden offshore flow in the land-breeze as an aerosol laden region which is roughly parallel to the shoreline of the lake. When

a sequence of the 10-m altitude cross sections are animated, motions of the aerosol structures inside the lake-breeze front show a westerly flow. With careful enhancement of this cross section we can also see aerosol inhomogeneities beyond the front moving in a easterly flow.

Between 15:24 and 16:46 UTC the lidar was aligned horizontally and scanned back-and-forth to produce PPI scans between an azimuth of 85° and 176°. These were acquired with an angular separation between profiles of 0.08° providing a scan time of 12 seconds. Animations of these scans show the position of the land breeze fluctuating in a series of surges and regressions. The outflow wind is made clearly evident by the motion of aerosol inhomogeneities. The signal strength was sufficient to provide usable images of the front out to $\sim$ 12 km south of the lidar. Visual observations during this period showed the lake to be calm without capillary waves near the shore. Offshore, at a distance which appeared consistent with the lidar imaged front, the water surface turned dark and disturbed by the on shore flow. Figure 6 presents wind speed and direction as a function of distance from shore. These measurements were obtained from the motion of aerosol inhomogeneities using algorithms presented by Pirronen and Eloranta, 1995; and Schols and Eloranta 1992. These winds are averaged over a period of 47 minutes and a north-south band extending from from 1 to 2 km south of the lidar. The measurements were taken $\sim$ 5 m above the lake surface.

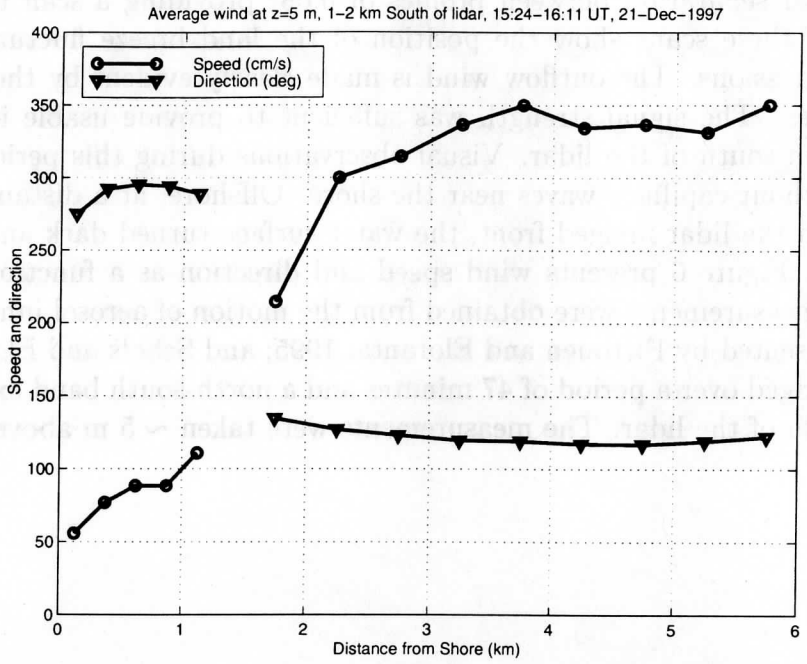

Figure 6. Wind speed and direction as a function of the distance from shore at 5 m above the lake surface. During the 47 min averaging period the front position oscillated slightly in the east-west direction. Winds are only plotted for positions which were always on the same side of the front. This produces a gap in the measurements at $\sim$ 1.5 km from shore.

Acknowledgments

This work was made possible by NSF grant number ATM9707165 and ARO grant number ARO DAAH-04-94-G-0195.

References

- Pirronen, A., K. and E. W. Eloranta, 1995: Accuracy analysis of wind profiles calculated from volume imaging lidar data, *J. of Geophysical Research*, **100**, 25559-25567.

- Schols, J. L., and E. W. Eloranta, 1992: The calculation of area-averaged vertical profiles of the horizontal wind velocity from volume imaging lidar data ., *J. of Geophysical Research*, **97**, 18395-18407.

Presented at the AMS Conference on Boundary Layers and Turbulence
Dallas, TX, Jan, 1999

Comparison of micro-scale convection patterns seen in lidar data and large-eddy simulations

Shane D. Mayor, Gregory J. Tripoli, Edwin W. Eloranta, and Bradley D. Hoggatt
Department of Atmospheric and Oceanic Sciences, University of Wisconsin
1225 W. Dayton St., Madison, Wisconsin, 53706, USA
phone: 608-263-6847, fax: 608-262-5974, e-mail: shane@lidar.ssec.wisc.edu

Introduction

Large eddy simulations (LESs) provide an attractive way of developing parameterizations for large-scale models such as global climate and weather forecast models. This is because they provide 4-D information which can potentially be used to compute fluxes with sampling errors that are much smaller than those made from in situ measurements. LESs, however, are only viable if we have confidence in their solutions. In particular, high resolution 4-D measurements are needed to test the LESs ability to accurately simulate the organization of convection such as linear and cellular boundary layer circulations. The objective of our research is to demonstrate the usefulness of volume imaging lidar data in LES validation.

To do this, we deployed the University of Wisconsin Volume Imaging Lidar (UW-VIL) at a site on the western edge of Lake Michigan and observed the growth of the convective boundary layer (CBL) over the water during cold-air outbreaks. We also ran the University of Wisconsin nonhydrostatic modeling system (UW-NMS) with microscale grid spacing to simulate lake-induced CBLs. This nonhomogeneous environment offers the advantages of a wide range of CBL depths and convective organization patterns within a simulation domain and requires substantially less computer time when compared to homogeneous CBL simulations that must be run for a large part of the diurnal cycle before several large-eddy turn-overs are obtained.

Previous work using VIL data to validate LES can be found in Avissar *et al.* 1998.

Observations

The UW-VIL was deployed in Sheboygan, Wisconsin, for the Lake-Induced Convection Experiment (Lake-ICE) during December of 1997 and January of 1998. The site (43°44′N, 87°42′W, 176 m ASL) was located within 10 m of the western shore of Lake Michigan. The VIL's beam-steering-unit (the point at which lidar beam is transmitted from) was located approximately 5 m above the lake surface. Thus, horizontal scans (PPIs) at 0° elevation allowed us to map the horizontal distribution of aerosol and steam-fog in a plane approximately 5 m above and parallel to the surface of the lake. Figure 1 is a PPI scan of this type. Steam-fog and hygroscopic aerosol produced a high-scattering tracer near the lake surface.

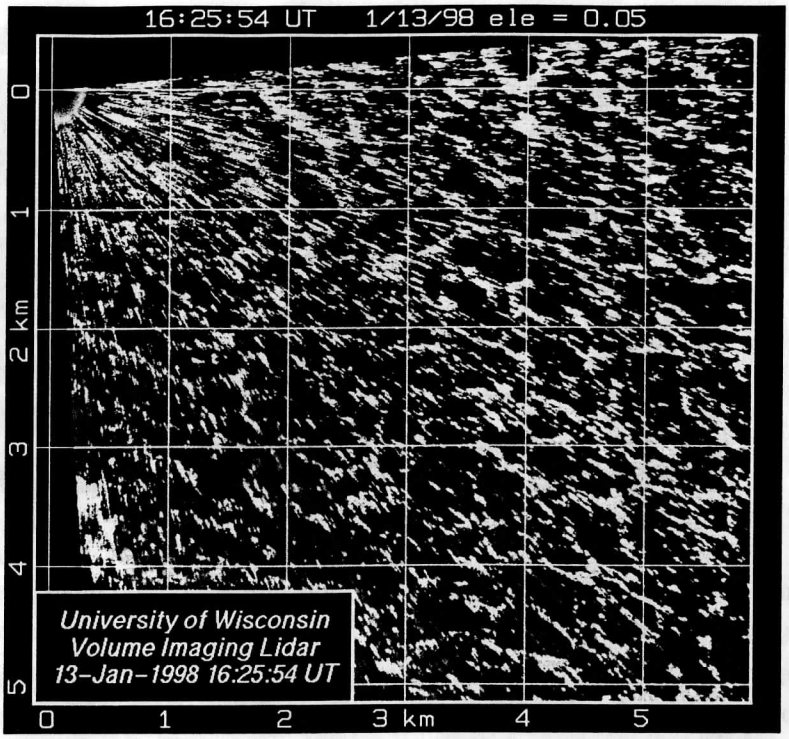

Figure 1. PPI of range-corrected backscatter intensity showing the organization of the steam-fog on 13 January 1998 from a few hundred meters to 5.9 km offshore. At the shore the mean wind during this time was from 280-290° at 5-10 m s^{-1} and the air temperature was -20° C. The open-cells range in horizontal size from about 100 m at 1 km offshore to about 500 m at 5.9 km offshore.

In addition to measuring aerosol scattering on horizontal slices through the surface layer, the VIL is capable of making vertical slices (RHIs) through the entire mixed layer and mapping the 3-D structure of aerosol scattering in the boundary layer. By rapidly moving the laser beam in a series of RHIs, each with a slightly increased azimuth angle, we can measure the 3-D structure. For example, a volume scan spanning 40° in azimuth and 15° in elevation angle requires about 2 minutes. A typical change in elevation angle between two laser pulses during an RHI is 0.23°. By repeating such volume scans, we can also monitor the temporal evolution of the structures.

Perhaps the most interesting VIL observations during Lake-ICE were open-cell patterns in the steam-fog about 5 meters above the surface of the lake on 10 and 13 January 1998. Cold air advection was occurring on both of these days and visual observations confirmed clear skies over the lidar site and steam fog on the surface of the lake. On 10 January the minimum temperature reached -16.7° C at 14 UTC with the wind from 236° at 6.5 m s^{-1}. On 13 January the air temperature dropped to -20° C and the wind was from 280-290° at 5-10 m s^{-1}. The lake water temperature on these days ranged from 3 to 5° C. In this paper we focus on the 13 January case, but we intend to present other cases at the poster.

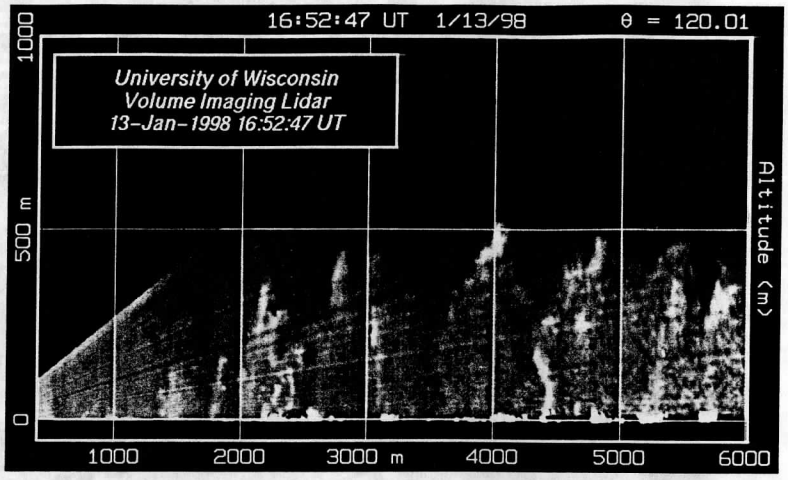

Figure 2. RHI of range-corrected backscatter intensity showing the vertical structure of steam-fog on 13 January 1998 from a couple hundred meters to 6 km offshore. Narrow columns of steam-fog and aerosol can be seen above the lake surface. A 500-m deep mixed layer formed over land appears to be advecting offshore which is also indicated in the upwind radiosonde sounding in figure 3.

The horizontal cell dimensions increase with increasing offshore distance and appear to be slightly elongated in the direction of the wind. Their somewhat hexagonal shape allows any one cell to share most of its walls with neighboring cells. Cell widths on the left side of figure 1 range from approximately 100 to 500 m while cell widths on the right range from 500 to 1000 m. The streaks across the image are caused by attenuation from the steam fog. While the steam on the 10th did not appear to rise more than about 50-m above the lake, RHI scans from 13 January, such as figure 2, reveal narrow rising columns of steam which sometimes extend to the top of a 500-m deep mixed-layer. The columns are very bright near the surface and decrease in intensity with altitude. In figure 2, there is one such feature at about 4.4 km range that extends from the surface up to about 200 m. Some of these features may be steam devils and we hope that the VIL observations of them will enable us to quantify their size and number density.

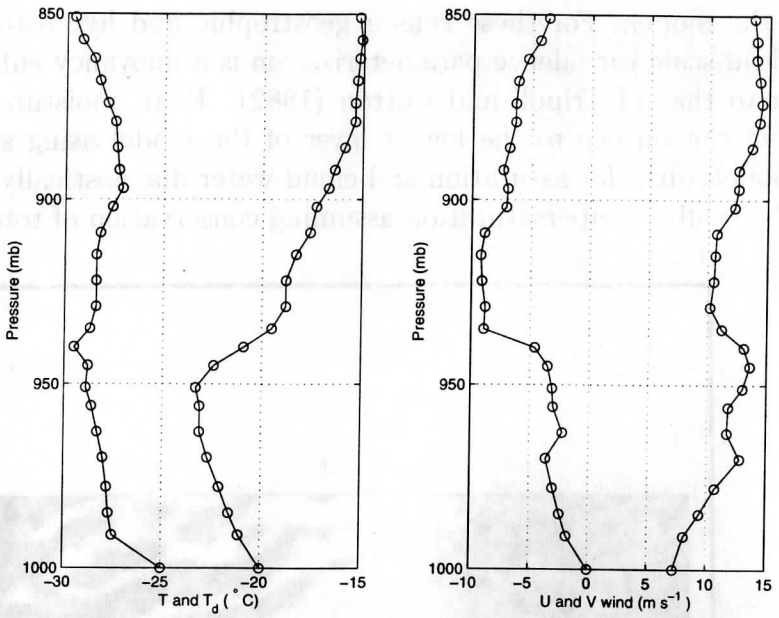

Figure 3. NCAR ISS CLASS sounding from 13 January 1998 at 16:30 GMT was used to initialize our model. The VIL also indicates a mixed layer extending up to about 500 m (about 950 mb) at the coast which is being advected over the lake by the larger scale flow. The wind profile shown here has been rotated so that the surface wind vector is normal to the north-south shoreline in the model.

Modeling

We are running the University of Wisconsin's scalable non-hydrostatic modeling system (Tripoli 1992) to simulate the leading edge of a lake-induced CBL. The model is a computationally efficient, elastic, fully non-Boussinesq grid-point model which includes enstrophy conservation.

For the work presented here, which represents our first attempts to simulate the lake-induced CBL, the model was run three times with horizontal resolutions of 10, 25 and 50 m. All of the simulations used a 0.25 s time-step and a vertical resolution of 1 m at the surface which increased at a rate of 1.1*dz until a resolution of 50 m was obtained (at about 450 m.) All simulations used 140x70x80 grid-points. The surface of the western 40 grid-points of each domain was snow-covered at air-temperature and the remaining surface was water at a temperature of 279 K.

The model was initialized with horizontally homogeneous initial conditions as prescribed by a radiosonde sounding 10 km upwind (figure 3). This profile of temperature, dew point and wind is maintained along the upwind (inflow at western wall) of the domain. Cyclic (periodic) boundary conditions are implemented along the northern and southern walls of the domain. An open boundary condition is maintained along the eastern wall (outflow). A Rayleigh absorbing layer of 16-points with a minimum dissipation time of 10 s was used

at the top of the model. For these runs a geostrophic and hydrostatic reference state is assumed. Subgrid-scale turbulence parameterization is a buoyancy enhanced eddy-viscosity closure similar to that of Tripoli and Cotton (1982). Heat, moisture and momentum are transferred from the surface to the lowest layer of the model using standard bulk mixing theory. The model solves for saturation and cloud water diagnostically and the steam fog is produced as the result of supersaturation assuming conservation of total water mixing ratio and entropy.

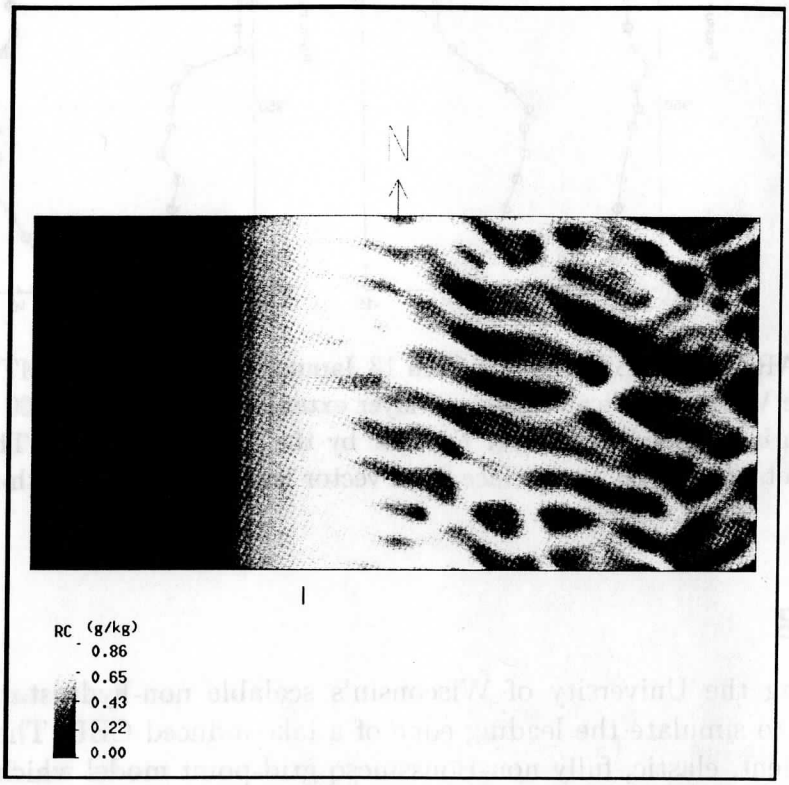

Figure 4. Horizontal distribution of condensed water (steam-fog in g/kg) at the lowest level of the model (1 m) at 30 minutes into simulation. The horizontal grid resolution was 50 m for this run. The size of the domain is 7 km (east-west) by 3.75 km (north-south).

The simulation with 50-m horizontal resolution, which has a horizontal domain of 7.0 by 3.5 km, produces a homogeneous region of steam-fog along the coastline out to approximately 1.5 km offshore where linear rolls form. The image shown in figure 4 is from 30 minutes after the beginning of the simulation—long after parcels entering the upwind edge of the domain would have traversed the full east-west distance of the domain. The flow near the surface veers with increasing offshore distance. At the downwind edge of the domain, the CBL depth has grown to approximately 600 m. When streamlines of the horizontal flow (such as those in figure 6) are superimposed on the condensed water field, the bands of steam-fog lie in regions of convergence and upward motion.

Figure 5 shows an east-west vertical slice of the lowest 15 grid-points at 30 minutes in the simulation. This image ranges from the surface to 26.2 m above the lake and is 7 km wide. The image shows the upward-sloping leading edge of the homogeneous band of steam-fog

shown in figure 4 and some narrow columns of steam-fog rising from the surface of the lake. These features, which would be visible wisps of steam fog in reality, can be compared to the very bright spots along the bottom edge of the RHI shown in figure 2. The narrow columns of scattering which sometimes extend to the top of the 500-m deep mixed layer in figure 2 are composed of visible steam fog just above the surface and hygroscopically swollen aerosols at the remaining levels.

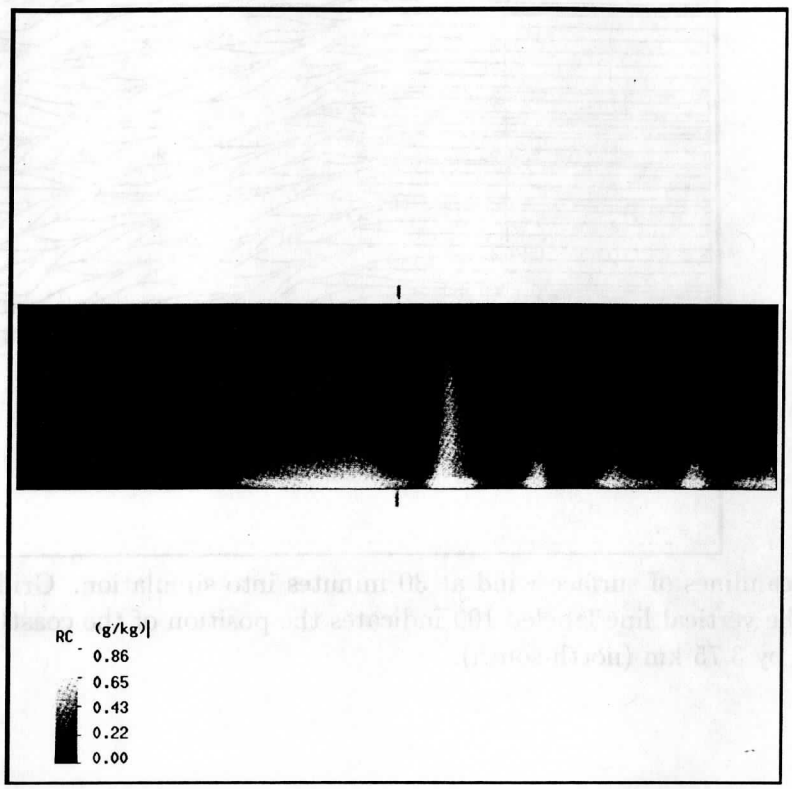

Figure 5. East-west vertical slice through the lowest 15 grid-points of the model domain showing condensed water (steam-fog in g/kg) at 30.0 minutes into simulation. The horizontal grid resolution was 50 m for this run. The image is 7 km wide by 26.2 m tall.

The 25 m and 10 m horizontal resolution simulations also use domains with 140x70x80 grid-points, and thus cover less area than the 50 m grid. The 25 m grid covers 3.5 by 1.75 km and the 10 m grid covers 1.4 km by 700 m. Both of these simulations produce a homogeneous region of steam-fog immediately downwind of the shoreline followed by linear rolls. Nine roll circulations set up in the 50 m grid (λ = 420 m); approximately 12 in the 25 m grid (λ=160 m), and 18 in the 10 m grid (λ = 40 m). The 50 m grid appears to preserve these roll structures downstream for a much greater proportion of the grid. Downstream of the rolls, a braided or more cellular appearing pattern, can be seen in all three simulations. The dependence of the structure on resolution warrants further investigation.

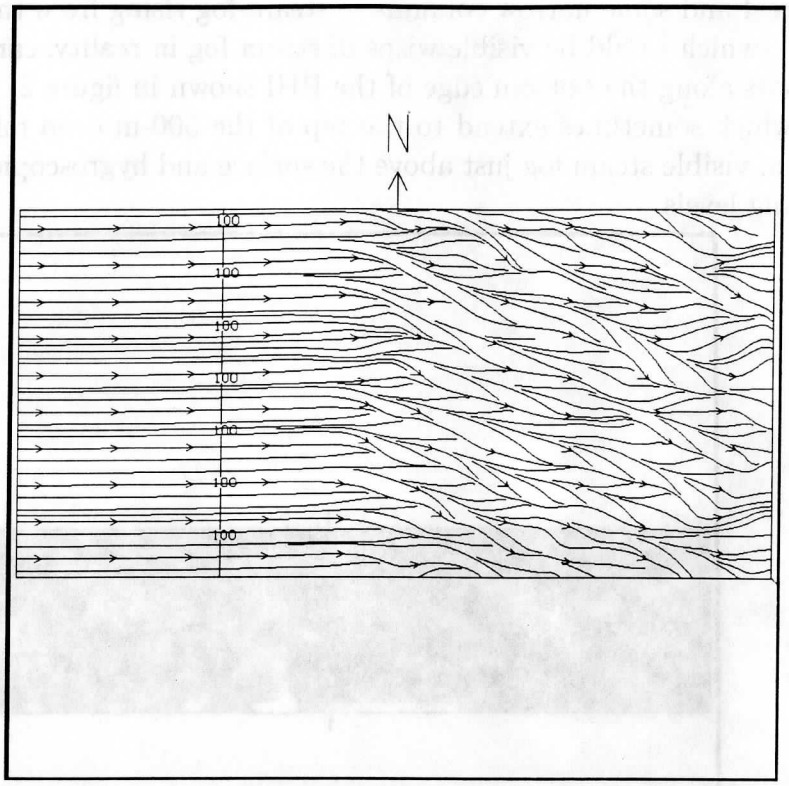

Figure 6. Streamlines of surface wind at 30 minutes into simulation. Grid resolution was 50 m for this run. The vertical line labeled 100 indicates the position of the coastline. This domain is 7 km (east-west) by 3.75 km (north-south).

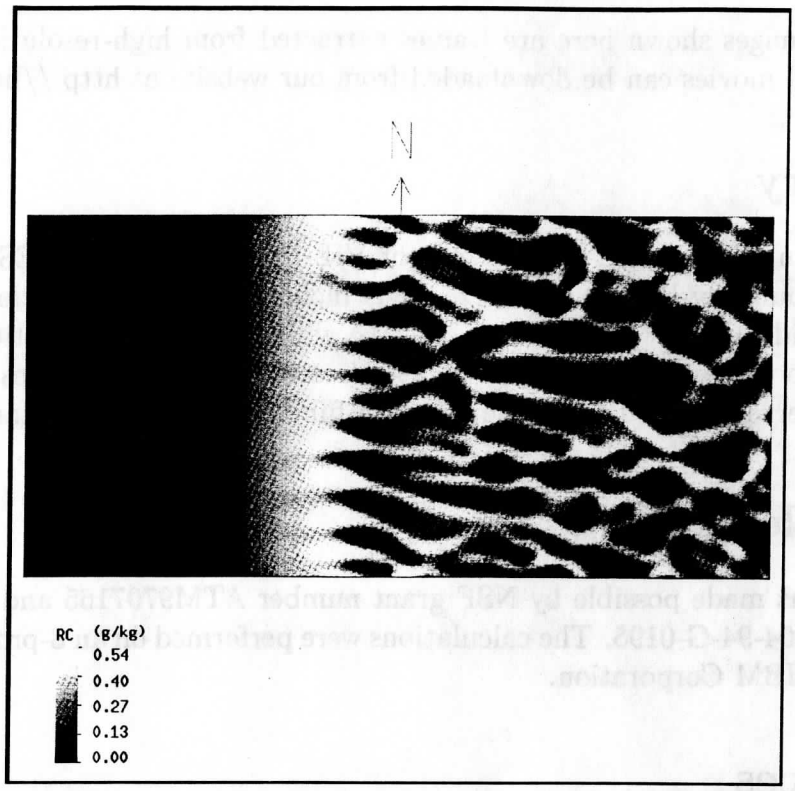

Figure 7. Same as in Figure 4 except with 25 m horizontal resolution and a 3.5 by 1.75 km domain.

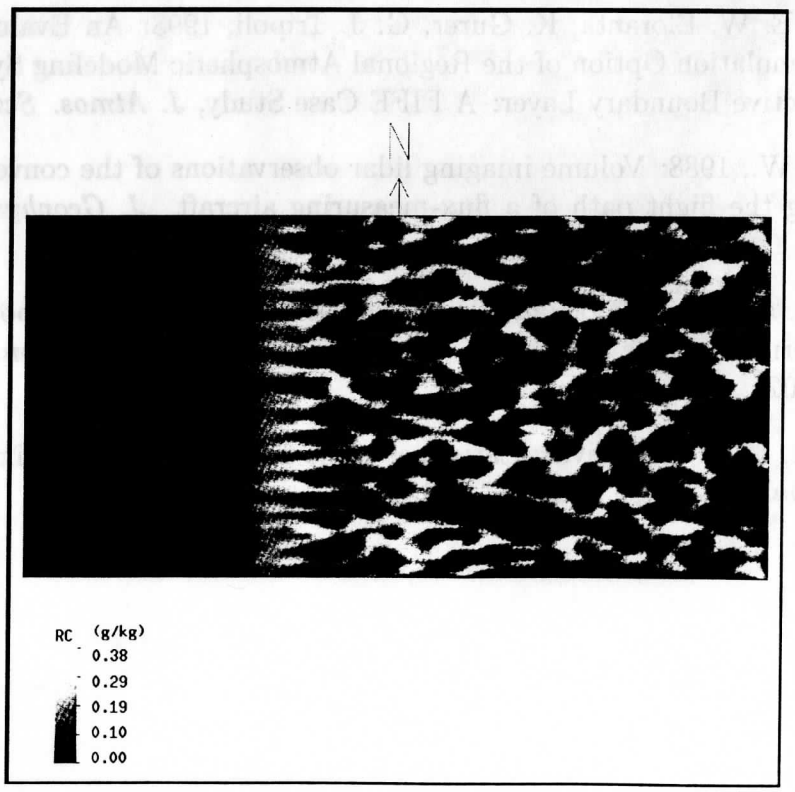

Figure 8. Same as in Figure 4 except with 10 m horizontal resolution and a 1.4 by 0.7 km domain.

All the images shown here are frames extracted from high-resolution color animations. These MPEG movies can be downloaded from our website at http://lidar.ssec.wisc.edu.

Summary

We have begun qualitative comparisons of VIL observations and LES of the lake-induced convective boundary layers. Our next steps include running simulations with high spatial resolution grids and very large domains. We will also perform quantitative comparison of wind fields; boundary layer depth; shapes, sizes and correlation times of the structures in both the observations and model output as a function of offshore distance.

Acknowledgements

This work was made possible by NSF grant number ATM9707165 and ARO grant number ARO DAAH-04-94-G-0195. The calculations were performed on an 8-processor J50 computer furnished by IBM Corporation.

References

Avissar, R., E. W. Eloranta, K. Gurer, G. J. Tripoli, 1998: An Evaluation of the Large-Eddy Simulation Option of the Regional Atmospheric Modeling System in Simulating a Convective Boundary Layer: A FIFE Case Study, *J. Atmos. Sci.*, **55**, 1109–1130.

Eloranta, E. W., 1988: Volume imaging lidar observations of the convective structure surrounding the flight path of a flux-measuring aircraft. *J. Geophys. Res.*, **97**, 18383–18393.

Tripoli, G. J. and W. R. Cotton, 1982: The use of ice-liquid water potential temperature as a thermodynamic variable in deep atmospheric models. *Mon. Wea. Rev.*, **109**, 1094–1102.

Tripoli, G. J., 1992: A nonhydrostatic mesoscale model designed to simulate scale interaction, *Mon. Wea. Rev.*, **120**, 1342–1359.